

Commun. Theor. Phys. **76** (2024) 035501 (13pp) https://doi.org/10.1088/1572-9494/ad23db

Cold plasma-induced effects on electromagnetic wave scattering in waveguides: a mode-matching analysis

Shahana Rizvi and Muhammad Afzal

Department of Mathematics, Capital University of Science and Technology, Islamabad, Pakistan

E-mail: dr.mafzal@cust.edu.pk

Received 7 September 2023, revised 29 January 2024
Accepted for publication 30 January 2024
Published 7 March 2024

Abstract

This article presents advancements in an analytical mode-matching technique for studying electromagnetic wave propagation in a parallel-plate metallic rectangular waveguide. This technique involves projecting the solution onto basis functions and solving linear algebraic systems to determine scattering amplitudes. The accuracy of this method is validated via numerical assessments, which involve the reconstruction of matching conditions and conservation laws. The study highlights the impact of geometric and material variations on reflection and transmission phenomena in the waveguide.

Keywords: electromagnetic waves, scattering, cold plasma, metallic conducting, mode-matching technique

(Some figures may appear in colour only in the online journal)

1. Introduction

Plasma, an electrically conducting quasi-neutral gas comprising charged particles that collectively move, also contains molecules and photons across various wavelengths. Plasma constitutes a major portion of the observable universe. Its charged particle motion facilitates the propagation of electromagnetic waves. The magnetosphere surrounding the Earth contains dense, cold plasma, causing electromagnetic waves interacting with the Earth's atmosphere to naturally serve as a source for radio communication. This specific type of plasma, found within the Earth's magnetosphere, is categorized as non-thermal due to the significantly higher temperature of electrons compared to ions and neutrals [1]. The non-thermal nature of cold plasma holds particular significance in biomedicine. It exhibits the capability to eliminate cancer cells and activate specific signaling pathways that are crucial in treatment responses, offering a novel and innovative approach to combat cancer [2]. Plasma-filled waveguides find application in converting methane into hydrogen or synthesis gas, essential for producing raw chemicals like methanol and ammonia, as well as functioning as hydrogenation agents in oil refineries and reducing gases in the steel industry [3].

Wait [4] explained that in the presence of a constant magnetic field, the dielectric constant of a plasma is in the form of a tensor. He gave explicit results for the reflection coefficients of stratified plasma in planar and cylindrical geometry.

Waveguides are structures that direct the propagation of energy in a channel. The variation of geometric settings and material properties has a significant impact on the scattering characteristics of the channel. Analytical mode-matching methods are found to be useful for analysis of the energy propagation in a waveguide. The technique has recently been advanced in various directions to investigate the scattering behavior of acoustic waves at structural discontinuities: for instance, see [5–10]. The transfer of electromagnetic energy using plasma waveguides has always been an interest of researchers [11–15]. A study of plasma waveguides shows that their properties differ, in many significant aspects, from those of conventional dielectric waveguides.

The scattering of microwaves propagating through a circular waveguide, partially filled with a homogeneous lossless and cold electron plasma, was studied by Gehre *et al*

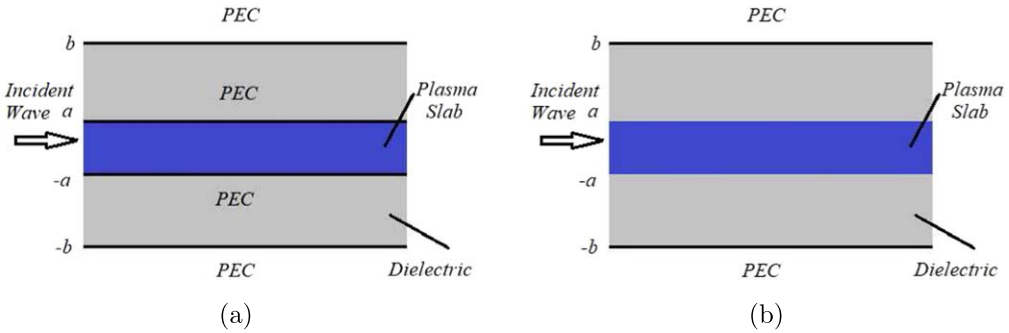

Figure 1. The cold plasma slab configuration: (a) enclosed by metal strips, and (b) embedded within a dielectric environment.

[16]. After finding the plasma dielectric tensor analytically, investigations were performed by Khalil and Mousa of the electromagnetic wave propagation in a plasma-filled cylindrical waveguide [17]. Dvorak *et al* [18] investigated the propagation of an ultra-wide-band electromagnetic pulse in a homogeneous cold plasma, and the reflection and absorption of a polarized wave in an inhomogeneous disspative magnetized plasma slab were investigated analytically by Jazi *et al* [19]. The solution to the scattering of plane electromagnetic waves by an anisotropic sphere with plasma was obtained by Geng *et al* [20]. A multiscale property in a Janus metastructure can be achieved by adjusting the incident angle of electromagnetic waves, by arranging the dielectrics asymmetrically, and by using the anisotropy of the plasma [21, 22]. The scattering of microwaves from a plasma column in a rectangular waveguide has also been discussed [23, 24].

To analyze the scattering of electromagnetic waves in cold plasma-filled waveguides, different numerical techniques have been applied [25–35]. The mode-matching technique is often applicable in solving discontinuity problems in isotropic waveguides [36]. This technique has been applied to write a high-frequency structure to analyze the program for the resonator of gyro-devices [37]. The electromagnetic wave transmission from a lossless isotropic cylindrical waveguide with metallic walls to a semi-bounded plasma, using the mode-matching technique, has also been analyzed [38]. Rao *et al* [39] observed that the total phase retarder bandwidth can reach 2.6 GHz by appropriately optimizing the incident angle, the plasma frequency, the external magnetic field and the nonlinear light intensity.

It is noted that the investigations conducted in most of the above-mentioned papers are restricted to cylindrical waveguides or circular columns in rectangular waveguides. With a few exceptions, the electromagnetic propagation in rectangular waveguides has not been widely discussed. Therefore, the originality of this work is the analysis of electromagnetic wave scattering in a parallel-plate waveguide, with a groove, containing a slab of cold unmagnetized plasma. To the best of our knowledge, this kind of attempt has not been made in the past. The solution of the problem has a significant purpose as waveguides are an integral part of resonators and plasma propulsion engines. This article provides a rigorous study of electromagnetic scattering in a two-dimensional parallel-plate rectangular waveguide, which contains a slab of cold plasma bounded by metallic strips, placed in a groove in the central region. The same physical configuration is discussed for a plasma slab placed, without strips, between layers of a dielectric.

The semi-analytic technique of mode matching is used to investigate electromagnetic wave scattering at discontinuities in the considered waveguide. It is a fast and convergent method, which can be applied easily without any discretization of variables. This technique provides an exact solution to electromagnetic scattering problems in both discontinuous and planar structures. In this work, the mode-matching method provides the solution for different parameters, frequencies and dimensions of heights of the cold plasma and dielectric media.

The article is arranged as follows: section 2 states the physical aspects of the problem and gives a brief description of the topic. In section 3, the eigenfunctions of the formulated boundary value problem are obtained by the governing Helmholtz equation and boundary conditions. The system thus obtained is solved numerically to calculate the transmission and reflection coefficients. The energy identity is proved in section 4. In section 5, simulations are performed for both frequency regimes, i.e. the transparency regime (the electromagnetic wave frequency is higher than the plasma frequency) and the non-transparency regime (the electromagnetic wave frequency is lower than the plasma frequency). Power analysis is also carried out for varying heights in both frequency regimes. The coefficients of reflection and transmission are also obtained with reference to the normalized wave frequency for transparency and non-transparency regions. Section 6 presents the summary and conclusions drawn for the two frequency regimes in dielectric and plasma regions.

2. Formulation of propagating waves within a plasma slab

The analysis of electromagnetic wave scattering discussed in this article is centered around a plasma slab, which is either enclosed between perfect electric conductor (PEC) plates or embedded within a dielectric medium. The physical configuration depicted in figure 1 represents the arrangement of the central region of the metallic waveguide in which the

scattering is analyzed. An $\boldsymbol{H}$-polarized incident wave is considered to be propagating in the positive x direction within this setting. This incident wave is assumed to be the fundamental duct mode, with unit amplitude, propagating from the left inlet to interfaces on the right. The incident angle is presumed to be making a zero angle with the x-axis. Copper or silver can be used as plates in this waveguide. In figure 1(a), the plasma slab is bounded by PEC walls, whereas in figure 1(b), the plasma slab is encompassed by a dielectric medium. The dimensions of the plasma slab adhere to the conditions $|y| < a$ and $|x| < L$, while the PEC walls in figure 1(a) are positioned at $y = \pm a, \pm b$, and in figure 1(b), the PEC walls are located at $y = \pm b$. The region between $|y| > a$ and $|y| < b$ is considered to be a dielectric medium with permittivity ϵ_0 and permeability μ_0. This configuration corresponds to a wave number k_0, which is defined as $k_0 = \omega\sqrt{\mu_0\epsilon_0}$, where ω represents the angular frequency and c denotes the speed of light, expressed as $c = \sqrt{1/\epsilon_0\mu_0}$. This relation implies that k_0 can be expressed as $k_0 = \omega/c$. However, for a cold plasma, the permeability remains μ_0, and the permittivity tensor $\overline{\epsilon}$, as specified in [40] and [41], is

$$\overline{\epsilon} = \begin{bmatrix} \epsilon_1 & -\mathrm{i}\epsilon_2 & 0 \\ \mathrm{i}\epsilon_2 & \epsilon_1 & 0 \\ 0 & 0 & \epsilon_3 \end{bmatrix},$$

where $\epsilon_1 = 1 - \dfrac{\omega_\mathrm{p}^2}{\omega^2 - \omega_\mathrm{c}^2}$, $\epsilon_2 = \dfrac{\omega_\mathrm{c}\omega_\mathrm{p}^2}{\omega(\omega^2 - \omega_\mathrm{c}^2)}$ and $\epsilon_3 = 1 - \dfrac{\omega_\mathrm{p}^2}{\omega^2}$. Here, the quantities ω_p and ω_c stand for the frequencies associated with plasma and cyclotron effects, respectively. The exponential temporal variation $\mathrm{e}^{-\mathrm{i}\omega t}$ is considered and consistently omitted [42].

Maxwell's equations dictate the propagation of electromagnetic waves in a waveguide. Faraday's law, presented below, remains valid for both dielectric and cold plasma mediums:

$$\nabla \times \boldsymbol{E} = \mathrm{i}\omega\boldsymbol{B}. \tag{1}$$

The expression of Ampere's law within the context of dielectrics is as follows:

$$\nabla \times \boldsymbol{B} = -\mathrm{i}\frac{\omega}{c^2}\boldsymbol{E}, \tag{2}$$

while in a cold plasma, this law is formulated as:

$$\nabla \times \boldsymbol{B} = -\frac{\mathrm{i}}{\omega}k_0^2\,\overline{\epsilon}.\boldsymbol{E}. \tag{3}$$

For a two-dimensional waveguide ($\partial/\partial z = 0$), the electromagnetic fields $\boldsymbol{E}$ and $\boldsymbol{B}$ include longitudinal components E_z and B_z and transverse components E_x, E_y, B_x and B_y. For electromagnetic wave propagation, the Maxwell's equations are solved together with boundary and interface conditions. In a dielectric, the longitudinal components satisfy the Helmholtz equation

$$\left(\frac{\partial^2}{\partial x^2} + \frac{\partial^2}{\partial y^2} + k_0^2\right)\begin{pmatrix} E_z \\ B_z \end{pmatrix} = \begin{pmatrix} 0 \\ 0 \end{pmatrix}, \tag{4}$$

whereas the transverse components can be found using the information from the longitudinal components, as given below:

$$E_x = -\frac{c^2}{\mathrm{i}\omega}\frac{\partial B_z}{\partial y}, \quad E_y = \frac{c^2}{i\omega}\frac{\partial B_z}{\partial x},$$
$$B_x = \frac{1}{i\omega}\frac{\partial E_z}{\partial y}, \quad B_y = -\frac{1}{i\omega}\frac{\partial E_z}{\partial x}.$$

For cold unmagnetized plasma, the Helmholtz equation is expressed, in longitudinal components of fields, as [43]

$$\left(\frac{\partial^2}{\partial x^2} + \frac{\partial^2}{\partial y^2} + k_\mathrm{I}^2\right)\begin{pmatrix} E_z \\ B_z \end{pmatrix} = \begin{pmatrix} 0 \\ 0 \end{pmatrix}. \tag{5}$$

The transverse components can be given as

$$E_x = \frac{\mathrm{i}\omega}{k_\mathrm{I}^2}\frac{\partial B_z}{\partial y}, \quad E_y = -\frac{i\omega}{k_\mathrm{I}^2}\frac{\partial B_z}{\partial x},$$
$$B_x = \frac{1}{i\omega}\frac{\partial E_z}{\partial y}, \quad B_y = -\frac{1}{i\omega}\frac{\partial E_z}{\partial x}.$$

The wave number of cold plasma medium is indicated as $k_\mathrm{I} = \dfrac{\omega}{c}\sqrt{1 - \dfrac{\omega_\mathrm{p}^2}{\omega^2}}$, where ω_p is the plasma frequency.

In the presence of a magnetic field, like the case of upper atmosphere, the cyclotron frequency ω_c is nonzero. All the components of the permittivity tensor $\overline{\epsilon}$ are present, which significantly affect the Helmholtz equation and transverse components of the electric field. Hence, the matching conditions are transformed. To determine the wave propagation in the regions presented in figure 1, equations (4) and (5) are solved subject to boundary and interface conditions. For an $\boldsymbol{H}$-polarized setting, the traveling wave formulation is explained in the next subsection.

2.1. Plasma slab enclosed by metal strips

For plasma in metallic strips, the PEC boundary conditions at the walls $y = \pm a$ and $\pm b$ are as

$$\frac{\partial B_z}{\partial y}(x, \pm a) = 0 = \frac{\partial B_z}{\partial y}(x, \pm b). \tag{6}$$

Upon solving equation (5), subject to equation (6) with the separation of the variable technique, the eigenfunction expansion formation can be achieved as:

$$B_z(x, y) = \begin{cases} \displaystyle\sum_{n=0}^{\infty}(B_n^{(1)}\mathrm{e}^{\mathrm{i}\zeta_n x} + C_n^{(1)}\mathrm{e}^{-\mathrm{i}\zeta_n x})Y_{1n}(y), \\ \displaystyle\sum_{n=0}^{\infty}(B_n^{(2)}\mathrm{e}^{\mathrm{i}\lambda_n x} + C_n^{(2)}\mathrm{e}^{-\mathrm{i}\lambda_n x})Y_{2n}(y), \\ \displaystyle\sum_{n=0}^{\infty}(B_n^{(3)}\mathrm{e}^{\mathrm{i}\zeta_n x} + C_n^{(3)}\mathrm{e}^{-\mathrm{i}\zeta_n x})Y_{3n}(y), \end{cases} \tag{7}$$

where $B_n^{(j)}$ and $C_n^{(j)}$, $j = 1, 2, 3$ exhibit the amplitudes in the respective regions $-b < y < -a$, $a < y < a$ and $a < y < b$. The wave numbers of nth modes in these regions are $\zeta_n = \sqrt{k_0^2 - \left(\dfrac{n\pi}{b-a}\right)^2}$ and $\lambda_n = \sqrt{k_\mathrm{I}^2 - \left(\dfrac{n\pi}{2a}\right)^2}$, $n = 0, 1, 2,$

… Here, the eigenfunctions $Y_{1n}(y) = \cos\left\{\left(\frac{n\pi}{b-a}\right)(y+b)\right\}$, $Y_{2n}(y) = \cos\left\{\left(\frac{n\pi}{2a}\right)(y+a)\right\}$ and $Y_{3n}(y) = \cos\left\{\left(\frac{n\pi}{b-a}\right)(y-b)\right\}$ are orthogonal and satisfy the usual orthogonality relations,

$$\left.\begin{aligned}\int_{-b}^{-a} Y_{1m}Y_{1n}\mathrm{d}y = \delta_{mn}\left(\frac{b-a}{2}\right)\epsilon_m,\\ \int_{-a}^{a} Y_{2m}Y_{2n}\mathrm{d}y = \delta_{mn}a\epsilon_m,\\ \int_{a}^{b} Y_{3m}Y_{3n}\mathrm{d}y = \delta_{mn}\left(\frac{b-a}{2}\right)\epsilon_m,\end{aligned}\right\} \tag{8}$$

where δ_{mn} is the Kronecker delta and $\epsilon_m = 2$ for $m = 0$ and 1 otherwise.

2.2. Plasma slab embedded within a dielectric environment

For a slab embedded within a dielectric environment, the interface and PEC boundary conditions are as follows

$$B_z(x, -a^-) = B_z(x, -a^+), \tag{9}$$

$$B_z(x, a^-) = B_z(x, a^+), \tag{10}$$

$$\eta_0\frac{\partial B_z}{\partial y}(x, -a^-) = \eta_1\frac{\partial B_z}{\partial y}(x, -a^+), \tag{11}$$

$$\eta_1\frac{\partial B_z}{\partial y}(x, a^-) = \eta_0\frac{\partial B_z}{\partial y}(x, a^+), \tag{12}$$

$$\frac{\partial B_z}{\partial y}(x, \pm b) = 0, \tag{13}$$

where the respective surface impedances of dielectric and cold plasma, η_0 and η_1, are related to wave numbers in these mediums as $\eta_0 = 1/k_0^2$ and $\eta_1 = 1/k_1^2$. Upon solving equation (5) subject to equations (10)–(14) with the separation of the variable technique, the eigenfunction expansion formation can be achieved as

$$B_z(x, y) = \sum_{n=0}^{\infty}(B_n\mathrm{e}^{\mathrm{i}s_nx} + C_n\mathrm{e}^{-\mathrm{i}s_nx})Y_n(y), \tag{14}$$

where B_n and C_n represent the amplitudes of the nth mode. The eigenfunction $Y_n(y)$ in the groove can be manifested as,

$$Y_n(y) = \begin{cases}Y_{1n}(y), & -b < y < -a,\\ Y_{2n}(y), & -a < y < a,\\ Y_{3n}(y), & a < y < b,\end{cases} \tag{15}$$

where

$$Y_{1n}(y) = \cosh[\tau_n(y+b)], \tag{16}$$

$$\begin{aligned}Y_{2n}(y) = {}& \frac{1}{\eta_1\gamma_n}\\ &\times\{\eta_0\tau_n\sinh[\tau_n(b-a)]\sinh[\gamma_n(y+a)]\}\\ &+\cosh[\tau_n(b-a)]\cosh[\gamma_n(y+a)],\end{aligned} \tag{17}$$

$$\begin{aligned}Y_{3n}(y) = {}& \frac{\cosh[\tau_n(y-b)]}{\eta_1\gamma_n\cosh[\tau_n(b-a)]}\{\eta_0\tau_n\\ &\times\sinh[\tau_n(b-a)]\sinh(2\gamma_na)\}\\ &+\eta_1\gamma_n\cosh[\tau_n(y-b)]\cosh(2\gamma_na),\end{aligned} \tag{18}$$

satisfy the orthogonality relation as given below

$$\begin{aligned}&\eta_0\int_{-b}^{-a} Y_{1m}Y_{1n}\mathrm{d}y + \eta_1\int_{-a}^{a} Y_{2m}Y_{2n}\mathrm{d}y\\ &+\eta_0\int_{a}^{b} Y_{3m}Y_{3n}\mathrm{d}y = \delta_{mn}E_m,\end{aligned} \tag{19}$$

where

$$\begin{aligned}E_n = {}&\eta_0\int_{-b}^{-a} Y_{1n}^2\mathrm{d}y + \eta_1\\ &\times\int_{-a}^{a} Y_{2n}^2\mathrm{d}y + \eta_0\int_{a}^{b} Y_{3n}^2\mathrm{d}y.\end{aligned} \tag{20}$$

The quantities τ_n and γ_n, written as $\tau_n = \sqrt{s_n^2 - k_0^2}$ and $\gamma_n = \sqrt{s_n^2 - k_1^2}$, represent the roots of the characteristic equation,

$$\begin{aligned}&\eta_0^2\tau_n^2\sinh^2[\tau_n(b-a)]\sinh(2\gamma_na) + \eta_1^2\gamma_n^2\\ &\times\cosh^2[\tau_n(b-a)]\sinh(2\gamma_na)\\ &+\eta_0\eta_1\tau_n\gamma_n\sinh[2\tau_n(b-a)]\cosh(2\gamma_na) = 0.\end{aligned} \tag{21}$$

Here, s_n indicates the wave number of the nth mode inside the groove.

3. Scattering from plasma slab: a mode-matching formulation

Within this context, the plasma slabs discussed in the preceding section are applied within the central segment ($|x| < L$) of the waveguide that extends infinitely along the x-axis. The physical arrangement of both cases is depicted in figure 2. The study involves the analysis of the scattering of electromagnetic waves by the plasma slab, by considering their initiation from the region at $x < -L$ and their subsequent interaction with the plasma-contained region as they exit the domain at $x > L$.

We contemplate an incident $\boldsymbol{H}$-polarized wave, propagating within this partially confined waveguide, in the positive x direction. The complete magnetic field, denoted by the field potential $B_z^{(T)}(x, y)$, is expressed as follows:

$$B_z^{(T)}(x, y) = \begin{cases}B_z^{(1)}(x, y), & x < -L, \quad -h < y < h,\\ B_z^{(2)}(x, y), & |x| < L, \quad -b < y < b,\\ B_z^{(3)}(x, y), & x > L, \quad -h < y < h.\end{cases} \tag{22}$$

Utilizing the mode-matching technique involves establishing the eigenfunction expansions and corresponding orthogonality criteria within each distinct region of the waveguide.

By employing a variable separable approach, the scattered fields within the regions $x < -L$ and $x > L$ can be demonstrated to take on the following representation:

$$\begin{aligned}B_z^{(1)}(x, y) = {}&\mathrm{e}^{\mathrm{i}k_0(x+L)} + \sum_{n=0}^{\infty}A_n\mathrm{e}^{-\mathrm{i}\nu_n(x+L)}\phi_n(y),\\ &-h < y < h,\end{aligned} \tag{23}$$

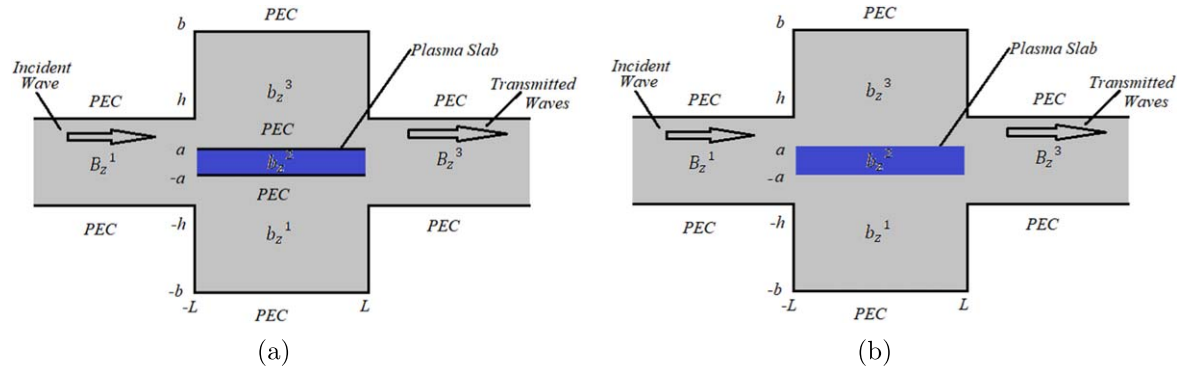

Figure 2. The waveguide configuration: (a) enclosed by metal strips, and (b) embedded within a dielectric environment.

$$B_z^{(3)}(x, y) = \sum_{n=0}^{\infty} D_n e^{i\nu_n(x-L)}\phi_n(y), \quad -h < y < h. \tag{24}$$

Here, ν_n, with n taking values of 0, 1, 2, and so forth, represents the wave number of the nth mode within the regions $x < -L$ and $x > L$. The amplitudes A_n and D_n define the strengths of these modes, while the eigenfunctions $\phi_n(y)$ can be expressed as,

$$\phi_n(y) = \cosh\left[\frac{n\pi}{2h}(y+h)\right].$$

These fields satisfy the Helmholtz equation and boundary conditions on perfectly conducting walls.

The eigenexpansion of $B_z^{(2)}$ can be extracted from equations (7) and (14) for the plasma slab enclosed by metallic strips and for the slab embedded in a dielectric environment, respectively.

It is worthwhile to note that the amplitudes appearing in the eigenexpansions (7), (14), (23) and (24) are unknowns and can be determined by implementing the matching conditions at the two interfaces.

3.1. Matching conditions

The continuity of fields at the interfaces $x = -L$ and $x = L$ infers the following matching conditions,

$$B_z^{(p)}(\pm L, y) = B_z^{(2)}(\pm L, y), \quad -h \leqslant y \leqslant h, \tag{25}$$

$$\frac{\partial B_z^{(2)}}{\partial x}(\pm L, y) = \begin{cases} 0, & -b \leqslant y \leqslant -h, \\ \dfrac{\partial B_z^{(p)}}{\partial x}(\pm L, y), & -h \leqslant y \leqslant -a, \end{cases} \tag{26}$$

$$\frac{\partial B_z^{(2)}}{\partial x}(\pm L, y) = \frac{\eta_0}{\eta_1}\frac{\partial B_z^{(p)}}{\partial x}(\pm L, y), \quad -a \leqslant y \leqslant a, \tag{27}$$

$$\frac{\partial B_z^{(2)}}{\partial x}(\pm L, y) = \begin{cases} \dfrac{\partial B_z^{(p)}}{\partial x}(\pm L, y), & a \leqslant y \leqslant h, \\ 0, & h \leqslant y \leqslant b, \end{cases} \tag{28}$$

where $p = 1$ for the field at interface $x = -L$ and $p = 3$ at interface $x = L$.

3.2. Plasma slab enclosed by metal strips

Employing the matching conditions, equation (25), together with some mathematical rearrangements leads to

$$\begin{aligned} A_m = -\delta_{m0} &+ \frac{1}{\epsilon_m h}\sum_{n=0}^{\infty}(B_n^{(1)}e^{-i\zeta_n L} + C_n^{(1)}e^{i\zeta_n L})P_{mn} \\ &+ \frac{1}{\epsilon_m h}\sum_{n=0}^{\infty}(B_n^{(2)}e^{-i\lambda_n L} + C_n^{(2)}e^{i\lambda_n L})Q_{mn} \\ &+ \frac{1}{\epsilon_m h}\sum_{n=0}^{\infty}(B_n^{(3)}e^{-i\zeta_n L} + C_n^{(3)}e^{i\zeta_n L})R_{mn}, \end{aligned} \tag{29}$$

$$\begin{aligned} D_m = &\frac{1}{\epsilon_m h}\sum_{n=0}^{\infty}(B_n^{(1)}e^{i\zeta_n L} + C_n^{(1)}e^{-i\zeta_n L})P_{mn} \\ &+ \frac{1}{\epsilon_m h}\sum_{n=0}^{\infty}(B_n^{(2)}e^{i\lambda_n L} + C_n^{(2)}e^{-i\lambda_n L})Q_{mn} \\ &+ \frac{1}{\epsilon_m h}\sum_{n=0}^{\infty}(B_n^{(3)}e^{i\zeta_n L} + C_n^{(3)}e^{-i\zeta_n L})R_{mn}, \end{aligned} \tag{30}$$

where

$$P_{mn} = \int_{-h}^{-a}\phi_m(y)Y_{1n}(y)\mathrm{d}y,$$
$$Q_{mn} = \int_{-a}^{a}\phi_m(y)Y_{2n}(y)\mathrm{d}y,$$
$$R_{mn} = \int_{a}^{h}\phi_m(y)Y_{3n}(y)\mathrm{d}y.$$

Adding equations (29) and (30) leads to

$$\begin{aligned} \Psi_m^+ = -\delta_{m0} &+ \frac{2}{h\epsilon_m}\Bigg\{\sum_{n=0}^{\infty}\Phi_{1n}^+\cos(\zeta_n L)P_{mn} \\ &+ \Phi_{2n}^+\cos(\lambda_n L)Q_{mn} + \Phi_{3n}^+\cos(\zeta_n L)R_{mn}\Bigg\}, \end{aligned} \tag{31}$$

while subtracting equation (30) from equation (29) submits

$$\begin{aligned} \Psi_m^- = -\delta_{m0} &- \frac{2i}{h\epsilon_m}\Bigg\{\sum_{n=0}^{\infty}\Phi_{1n}^-\sin(\zeta_n L)P_{mn} \\ &+ \Phi_{2n}^-\sin(\lambda_n L)Q_{mn} + \Phi_{3n}^-\sin(\zeta_n L)R_{mn}\Bigg\}, \end{aligned} \tag{32}$$

where $\Psi_m^{\pm} = A_m \pm D_m$ and $\Phi_{jm}^{\pm} = B_m^{(j)} \pm C_m^{(j)}$, $j = 1, 2, 3$.

Deploying the conditions of equation (26) to equation (28) at the interface $x = L$ capitulates

$$(B_m^{(1)}\mathrm{e}^{-\mathrm{i}\zeta_m L} - C_m^{(1)}\mathrm{e}^{\mathrm{i}\zeta_m L}) = \frac{2}{\zeta_m \epsilon_m (b-a)} \times \left\{k_0 P_{0m} - \sum_{n=0}^{\infty} A_n \nu_n P_{nm}\right\}, \tag{33}$$

$$(B_m^{(2)}\mathrm{e}^{-\mathrm{i}\lambda_m L} - C_m^{(2)}\mathrm{e}^{\mathrm{i}\lambda_m L}) = \frac{\eta_0}{\eta_1 \lambda_m \epsilon_m a} \times \left\{k_0 Q_{0m} - \sum_{n=0}^{\infty} A_n \nu_n Q_{nm}\right\}, \tag{34}$$

$$(B_m^{(3)}\mathrm{e}^{-\mathrm{i}\zeta_m L} - C_m^{(3)}\mathrm{e}^{\mathrm{i}\zeta_m L}) = \frac{2}{\zeta_m \epsilon_m (b-a)} \times \left\{k_0 R_{0m} - \sum_{n=0}^{\infty} A_n \nu_n R_{nm}\right\}. \tag{35}$$

Again, employing the matching conditions of equations (26) to (28) in the same above-mentioned manner, displays

$$(B_m^{(1)}\mathrm{e}^{\mathrm{i}\zeta_m L} - C_m^{(1)}\mathrm{e}^{-\mathrm{i}\zeta_m L}) = \frac{2}{\zeta_m \epsilon_m (b-a)} \sum_{n=0}^{\infty} D_n \nu_n P_{nm}, \tag{36}$$

$$(B_m^{(2)}\mathrm{e}^{\mathrm{i}\lambda_m L} - C_m^{(2)}\mathrm{e}^{-\mathrm{i}\lambda_m L}) = \frac{\eta_0}{\eta_1 \lambda_m \epsilon_m a} \sum_{n=0}^{\infty} D_n \nu_n Q_{nm}, \tag{37}$$

$$(B_m^{(3)}\mathrm{e}^{\mathrm{i}\zeta_m L} - C_m^{(3)}\mathrm{e}^{-\mathrm{i}\zeta_m L}) = \frac{2}{\zeta_m \epsilon_m (b-a)} \sum_{n=0}^{\infty} D_n \nu_n R_{nm}. \tag{38}$$

Subtracting equations (33) from (36), (34) from (37) and (35) from (38) leads to the formation of the following equations

$$\Phi_{1m}^{+} = \frac{\mathrm{i}}{\zeta_m \epsilon_m \sin(\zeta_m L)(b-a)} \times \left(k_0 P_{0m} - \sum_{n=0}^{\infty} \Psi_n^{+} \nu_n P_{nm}\right), \tag{39}$$

$$\Phi_{2m}^{+} = \frac{\mathrm{i}\eta_0}{2\eta_1 \lambda_m \epsilon_m a \sin(\lambda_m L)} \times \left(k_0 Q_{0m} - \sum_{n=0}^{\infty} \Psi_n^{+} \nu_n Q_{nm}\right), \tag{40}$$

$$\Phi_{3m}^{+} = \frac{\mathrm{i}}{\zeta_m \epsilon_m \sin(\zeta_m L)(b-a)} \times \left(k_0 R_{0m} - \sum_{n=0}^{\infty} \Psi_n^{+} \nu_n R_{nm}\right). \tag{41}$$

Now, respective adding of equations (33) and (36), (35) and (37), and (36) and (38) forms Φ_{1m}^{-}, Φ_{2m}^{-} and Φ_{3m}^{-} in the following way

$$\Phi_{1m}^{-} = \frac{1}{\zeta_m \epsilon_m \cos(\zeta_m L)(b-a)} \times \left(k_0 P_{0m} - \sum_{n=0}^{\infty} \Psi_n^{-} \nu_n P_{nm}\right), \tag{42}$$

$$\Phi_{2m}^{-} = \frac{\eta_0}{2\eta_1 \lambda_m \epsilon_m a \cos(\lambda_m L)} \times \left(k_0 Q_{0m} - \sum_{n=0}^{\infty} \Psi_n^{-} \nu_n Q_{nm}\right), \tag{43}$$

$$\Phi_{3m}^{-} = \frac{1}{\zeta_m \epsilon_m \cos(\zeta_m L)(b-a)} \times \left(k_0 R_{0m} - \sum_{n=0}^{\infty} \Psi_n^{-} \nu_n R_{nm}\right). \tag{44}$$

Equations (31), (32) and (39)–(44) reveal a system of infinite equations that have the unknowns $\{A_n, B_n^{(j)}, C_n^{(j)}, D_n\}$, $j = 1, 2, 3$. The system is truncated and is solved numerically, and the results will be explored in the numerical discussion section.

3.3. Plasma slab embedded within a dielectric environment

Aligning according to the matching conditions, equation (26), and normalization yields

$$A_m = -\delta_{m0} + \frac{1}{\epsilon_m h}\left\{\sum_{n=0}^{\infty}(B_n\mathrm{e}^{-\mathrm{i}s_n L} + C_n\mathrm{e}^{\mathrm{i}s_n L})(P_{mn} + Q_{mn} + R_{mn})\right\}, \tag{45}$$

$$D_m = -\frac{1}{\epsilon_m h}\left\{\sum_{n=0}^{\infty}(B_n\mathrm{e}^{\mathrm{i}s_n L} + C_n\mathrm{e}^{-\mathrm{i}s_n L})(P_{mn} + Q_{mn} + R_{mn})\right\}. \tag{46}$$

Adding equations (45) and (46) produces

$$\Psi_m^{+} = -\delta_{m0} + \frac{2}{h\epsilon_m}\sum_{n=0}^{\infty}\Phi_n^{+}\cos(s_n L)\{P_{mn} + Q_{mn} + R_{mn}\}, \tag{47}$$

and subtracting equation (46) from (45) results in

$$\Psi_m^{-} = -\delta_{m0} - \frac{2i}{h\epsilon_m}\sum_{n=0}^{\infty}\Phi_n^{-}\sin(s_n L)\{P_{mn} + Q_{mn} + R_{mn}\}, \tag{48}$$

where $\Psi_m^{\pm} = A_m \pm D_m$ and $\Phi_m^{\pm} = B_m \pm C_m$.

By applying the matching conditions, equations (26)–(28), and solving, we get

$$\sum_{n=0}^{\infty}(B_n\mathrm{e}^{-\mathrm{i}s_n L} - C_n\mathrm{e}^{\mathrm{i}s_n L})s_n\int_{-b}^{-a} Y_{1m}Y_{1n}\mathrm{d}y = k_0\int_{-h}^{-a} Y_{1m}\mathrm{d}y - \sum_{n=0}^{\infty} A_n\nu_n\int_{-h}^{-a} Y_{1m}\phi_n\mathrm{d}y. \tag{49}$$

$$\frac{\eta_1}{\eta_0}\sum_{n=0}^{\infty}(B_n\mathrm{e}^{-\mathrm{i}s_n L} - C_n\mathrm{e}^{\mathrm{i}s_n L})s_n\int_{-b}^{-a} Y_{2m}Y_{2n}\mathrm{d}y = k_0\int_{-h}^{-a} Y_{1m}\mathrm{d}y - \sum_{n=0}^{\infty} A_n\nu_n\int_{-h}^{-a} Y_{2m}\phi_n\mathrm{d}y, \tag{50}$$

$$\sum_{n=0}^{\infty}(B_n e^{-is_nL} - C_n e^{is_nL})s_n \int_{-b}^{-a} Y_{3m}Y_{3n}dy = k_0 \int_{-h}^{-a} Y_{3m}dy - \sum_{n=0}^{\infty} A_n\nu_n \int_{-h}^{-a} Y_{3m}\phi_n dy. \quad (51)$$

Adding equations (49), (50) and (51) and employing the orthogonality relation, equation (19), produces

$$B_m e^{-is_mL} - C_m e^{is_mL} = \frac{\eta_0}{s_m E_m} \times \{k_0(P_{0m} + Q_{0m} + R_{0m}) - \sum_{n=0}^{\infty} A_n\nu_n(P_{nm} + Q_{nm} + R_{nm})\}. \quad (52)$$

The implementation of the conditions in equations (26) to (28) at the other interface $x = L$ and adopting the same procedure exhibits

$$B_m e^{is_mL} - C_m e^{-is_mL} = \frac{\eta_0}{s_m E_m} \times \sum_{n=0}^{\infty} D_n\nu_n(P_{nm} + Q_{nm} + R_{nm}). \quad (53)$$

Subtracting equation (52) from (53) brings out

$$\Phi_m^+ = \frac{ik_0\eta_0}{2s_m E_m \sin(s_mL)}(P_{0m} + Q_{0m} + R_{0m}) - \frac{i\eta_0}{2s_m E_m \sin(s_mL)}\sum_{n=0}^{\infty}\Psi_n^+\nu_n(P_{nm} + Q_{nm} + R_{nm}), \quad (54)$$

while adding equations (52) and (53) creates

$$\Phi_m^- = \frac{k_0\eta_0}{2s_m E_m \cos(s_mL)}(P_{0m} + Q_{0m} + R_{0m}) - \frac{\eta_0}{2s_m E_m \cos(s_mL)}\sum_{n=0}^{\infty}\Psi_n^-\nu_n(P_{nm} + Q_{nm} + R_{nm}). \quad (55)$$

The system of infinite algebraic equations, with unknown coefficients $\{A_n, B_n, C_n, D_n\}$, is shaped by equations (47), (48), (54) and (55). This system is truncated, and a numerical solution is provided and discussed in the numerical results section.

4. Energy flux

The accuracy and convergence of an approximate solution are measurable through proper comprehension of the energy flux.

To calculate the energy propagating in duct regions, we use the power Poynting vector given by,

$$\text{Power} = \frac{1}{2}Re\left(\int_R E_y^* B_z dy\right), \quad (56)$$

where $(^*)$ represents a complex conjugate.

For the dielectric medium, the component E_y of the electric field can be expressed as

$$E_y = -\frac{1}{i\omega\epsilon_0}\frac{\partial B_z}{\partial x}, \quad (57)$$

while for the cold plasma

$$E_y = \frac{c^2\eta_1}{i\omega\eta_0}\frac{\partial B_z}{\partial x}. \quad (58)$$

Applying the Poynting vector, the quantification of the incident power P_i, P_r and P_t provides,

$$P_i = -\frac{k_0 h}{\omega\epsilon_0}, \quad (59)$$

$$P_r = \frac{h}{2\omega\epsilon_0}Re\left(\sum_{n=0}^{\infty}|A_n|^2\nu_n^*\epsilon_n\right), \quad (60)$$

$$P_t = -\frac{h}{2\omega\epsilon_0}Re\left(\sum_{n=0}^{\infty}|D_n|^2\nu_n^*\epsilon_n\right). \quad (61)$$

Since $Re(\nu_n^*) = Re(\nu_n)$, therefore, equations (60) and (61) take the form,

$$P_r = \frac{h}{2\omega\epsilon_0}Re\left(\sum_{n=0}^{\infty}|A_n|^2\nu_n\epsilon_n\right), \quad (62)$$

$$P_t = -\frac{h}{2\omega\epsilon_0}Re\left(\sum_{n=0}^{\infty}|D_n|^2\nu_n\epsilon_n\right). \quad (63)$$

The principle of conservation of energy states,

$$P_i + P_r = P_t.$$

Applying this principle yields

$$-\frac{k_0 h}{\omega\epsilon_0} + \frac{h}{2\omega\epsilon_0}Re\left(\sum_{n=0}^{\infty}|A_n|^2\nu_n\epsilon_n\right) = -\frac{h}{2\omega\epsilon_0}Re\left(\sum_{n=0}^{\infty}|D_n|^2\nu_n\epsilon_n\right). \quad (64)$$

Scaling the incident power P_i to unity, equation (64) is modified as

$$1 = \mathcal{E}_1 + \mathcal{E}_2, \quad (65)$$

where

$$\mathcal{E}_1 = \frac{1}{2k_0}Re\left(\sum_{n=0}^{\infty}|A_n|^2\nu_n\epsilon_n\right),$$

$$\mathcal{E}_2 = \frac{1}{2k_0}Re\left(\sum_{n=0}^{\infty}|D_n|^2\nu_n\epsilon_n\right).$$

5. Numerical results and discussion

In view of the discussion presented in the above sections, we now solve the physical problem numerically. The speed of light, $c = 3 \times 10^8$ m/s is chosen as the physical parameter. The magnetic field B_z is presented in figures through the field $\phi(x, y)$, stated as,

$$\phi(x,y) = \begin{cases} \phi_1(x,y), & x < -L, \quad -h < y < h, \\ \phi_2(x,y), & |x| < L, \quad -b < y < -a, \\ \phi_3(x,y), & |x| < L, \quad -a < y < a, \\ \phi_4(x,y), & |x| < L, \quad a < y < b, \\ \phi_5(x,y), & x > L, \quad -h < y < h. \end{cases}$$

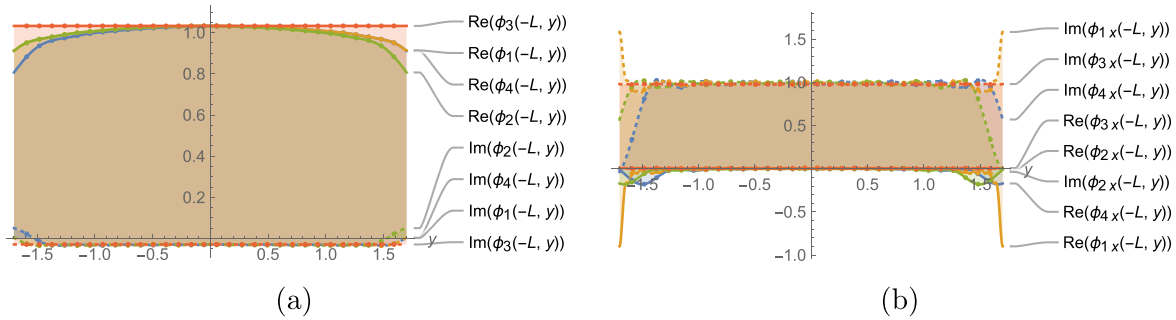

Figure 3. The real and imaginary parts of the (a) magnetic and (b) electric fields at $x = -L$, $-h < y < h$.

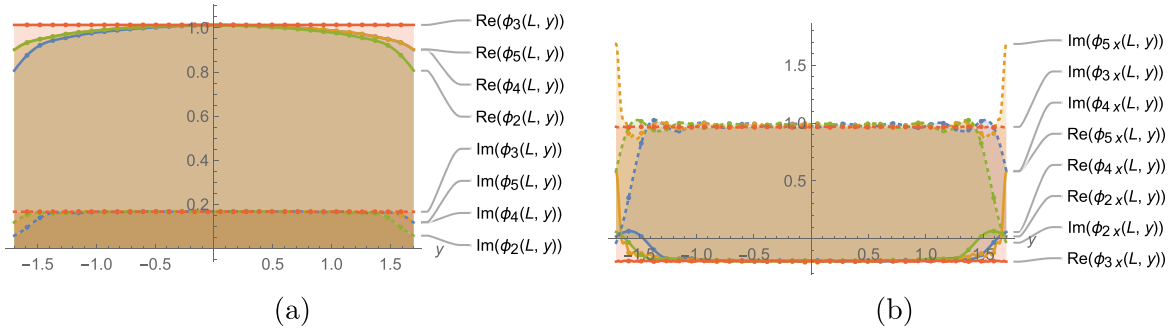

Figure 4. The real and imaginary parts of the (a) magnetic and (b) electric fields at $x = L$, $-h < y < h$.

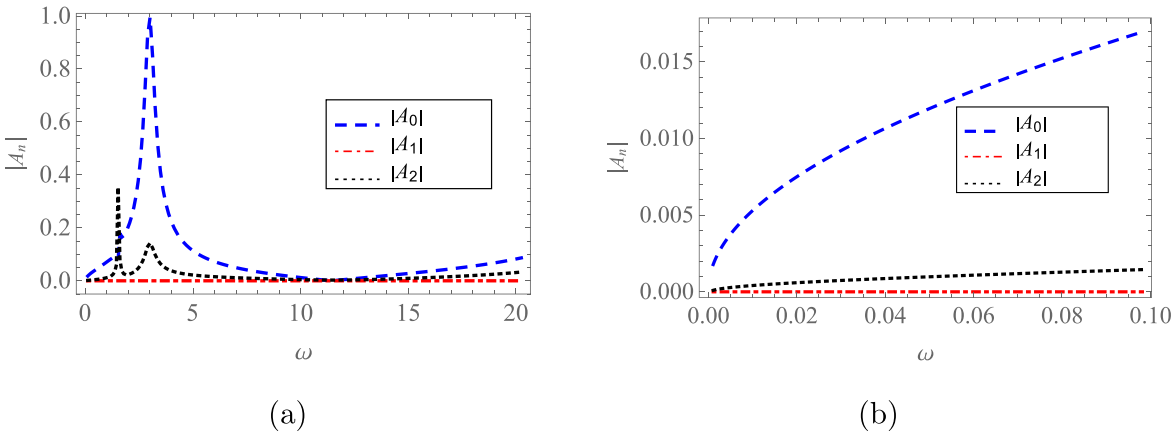

Figure 5. Reflected coefficients $|A_n|$ in the (a) transparency and (b) non-transparency regions.

The numerical calculations are carried out using the software Mathematica (versions 11.0 and 12.1).

5.1. Case I

After truncating the system divulged in equations (31), (32) and (39)–(44) up to 100 terms, the obtained solution is deployed to confirm the accuracy of algebra and power distribution. The matching conditions at the interfaces $x = -L$ and $x = L$ are thus reconstructed. The solution of these equations yields the unknown coefficients $\{A_n, B_n^{(j)}, C_n^{(j)}, D_n\}$, $j = 1, 2, 3$, $n = 0, 1, 2,\ldots,99$.

The incident duct modes ($n = 0, 1, 2$) of the scattered coefficients and the power distribution in duct regions are plotted against the normalized frequency $b\omega/c$.

Figures 3 and 4 present the validation of the mode-matching solution with the help of matching conditions of non-dimensional magnetic and electric fields at interfaces $x = -L$ and $x = L$, respectively.

The behavior of the first three incident modes of reflection and transmission coefficients against the normalized frequency $b\omega/c$ are presented in figures 5 and 6. It is worthwhile to mention that the region where the angular frequency ω is less than the plasma frequency ω_p is termed as the non-transparency region ($\omega < \omega_p$), and the region where ω is greater than ω_p is called the transparency region ($\omega > \omega_p$).

In terms of the normalized frequency, $b\omega/c$ is considered higher than 0.1 ($b\omega/c > 0.1$) in the transparency region, while it is lower than 0.1 ($b\omega/c < 0.1$) in the non-transparency region.

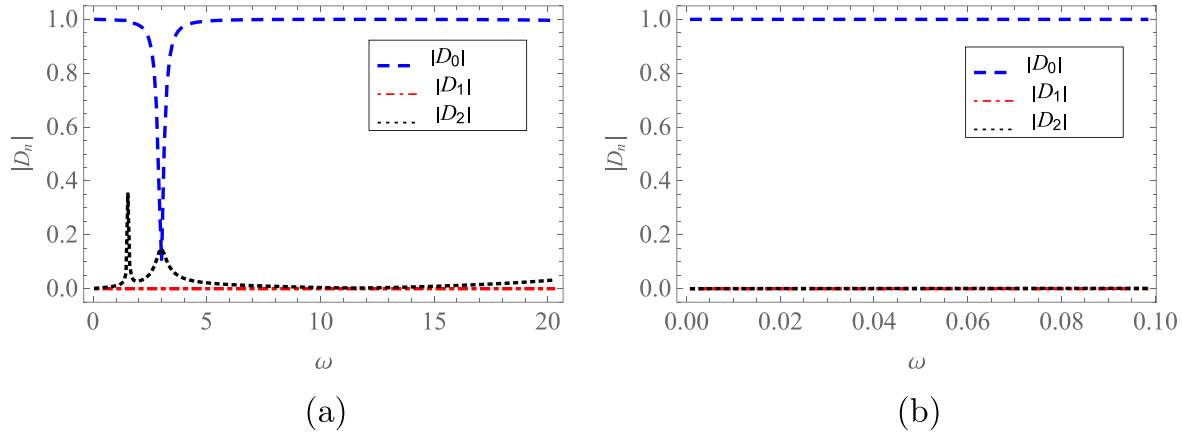

Figure 6. Transmitted coefficients $|D_n|$ in the (a) transparency and (b) non-transparency regions.

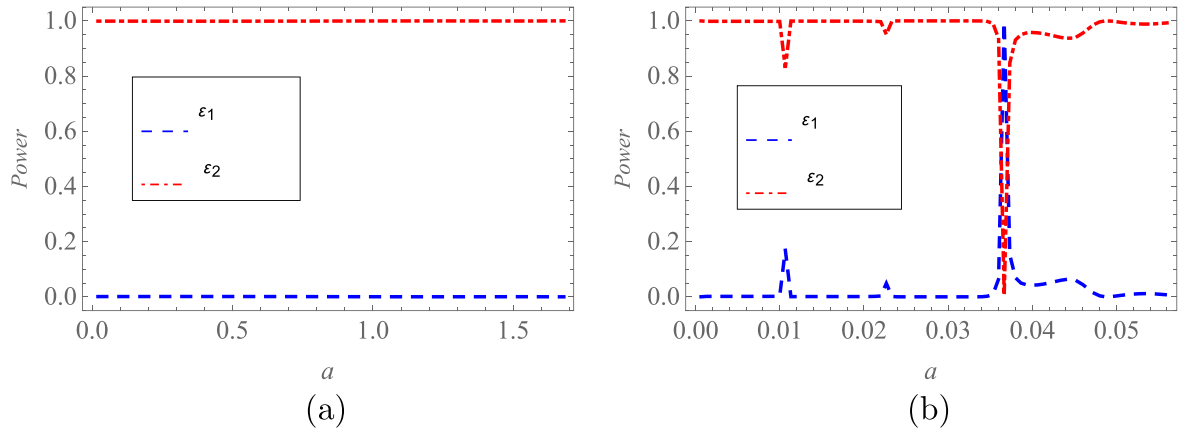

Figure 7. Power flux plotted against height a in (a) the transparency region and (b) the non-transparency region.

The graphs of reflected and transmitted powers are revealed in figures 7–9. The reflected power in the left duct ($x < -L$) is represented by $\mathcal{E}_1$. The quantity $\mathcal{E}_2$ is the transmitted power in the right duct ($x > L$). Here, $\mathcal{E}_t$ is the sum of powers in all duct regions,

$$\mathcal{E}_t = \mathcal{E}_1 + \mathcal{E}_2.$$

Figure 10 displays the plot of reflected and transmitted powers against the number of terms.

The relevant duct heights are set to $\bar{b} = 1$ cm, $\bar{a} = 0.004$ cm, $\bar{h} = 0.085$ cm. The length of the groove is fixed as $2\bar{L} = 2 \times 0.005$ cm, while the plasma frequency is fixed to be $\omega_p = 10^9$. The values of $\bar{a}$, $\bar{b}$ and ω_p are consistent with Najari *et al* [38]. The quantities a, b, h and L are the non-dimensional counterparts of $\bar{a}$, $\bar{b}$, $\bar{h}$ and $\bar{L}$, respectively. It is important to note that for all the plots other than the incident modes, the angular frequency is considered as $\omega = 6 \times 10^9$.

The reconstruction of matching conditions of the magnetic field ϕ_i and the electric field $\phi_{ix} = \dfrac{\partial \phi_i}{\partial x}$, $i = 1, 2, 3, 4$ at the interface $x = -L$ is shown in figures 3(a) and (b). The real and imaginary parts of these fields completely coincide at this interface. Figure 4(a) indicates the excellent agreement of real and imaginary parts of the magnetic field ϕ_j, $j = 2, 3, 4, 5$, while figure 4(b) shows cogency of these components of the electric field $\phi_{jx} = \dfrac{\partial \phi_j}{\partial x}$ at the interface $x = L$.

Upon analyzing the graphs of incident modes of reflection coefficients, in terms of the normalized frequency, it is noted that the first mode remains dominant and the second mode remains insignificant for both the transparency (figure 5(a)), and non-transparency (figure 5(b)) regimes.

The transmission coefficients plotted for the first three consecutive modes in the transparency (figure 6(a)) and non-transparency (figure 6(b)) frequency regions show that in both regimes, the transmitted mode number 1 remains dominant. Mode 2 displays insignificant behavior.

Cut-on modes with respect to the heights a, b and h, in all regions of the waveguide, for the transparency regime are also calculated. Region 1 represents the left duct $x < -L$, $|y| \leqslant h$. The regions $-b \leqslant y \leqslant -a$ or $a \leqslant y \leqslant b$ in $|x| < L$ are represented as region 2, while region $-a \leqslant y \leqslant a$, comprising cold plasma, is considered as region 3. The right duct $x > L$, $|y| \leqslant h$ is considered as region 4.

With the increase in height h, regions 1 and 4 exhibit two cut-on modes. In region 2, the dielectric has five while, in region 3, cold plasma has only one cut-on mode. Tables 1 and 2 represent the cut-on modes with respect to heights a and b,

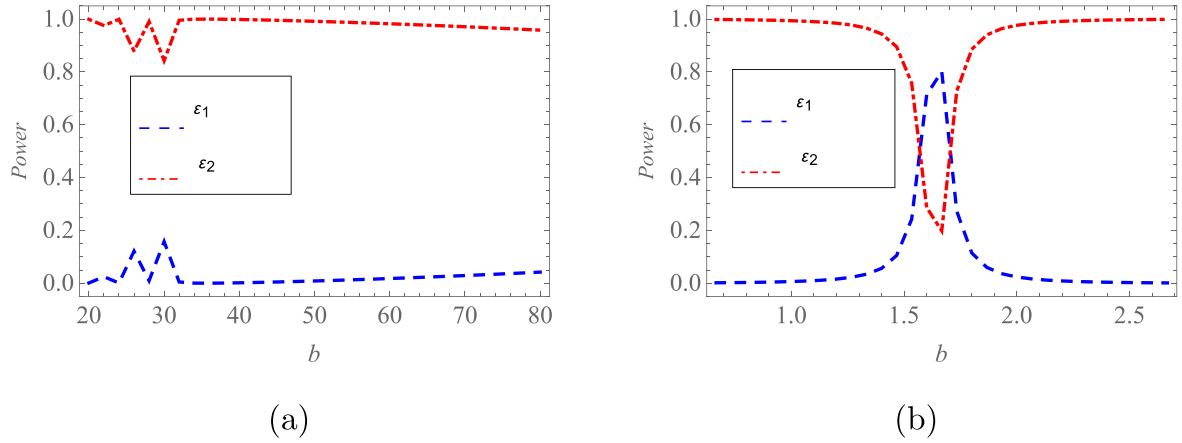

Figure 8. Power flux plotted against height b in (a) the transparency region and (b) the non-transparency region.

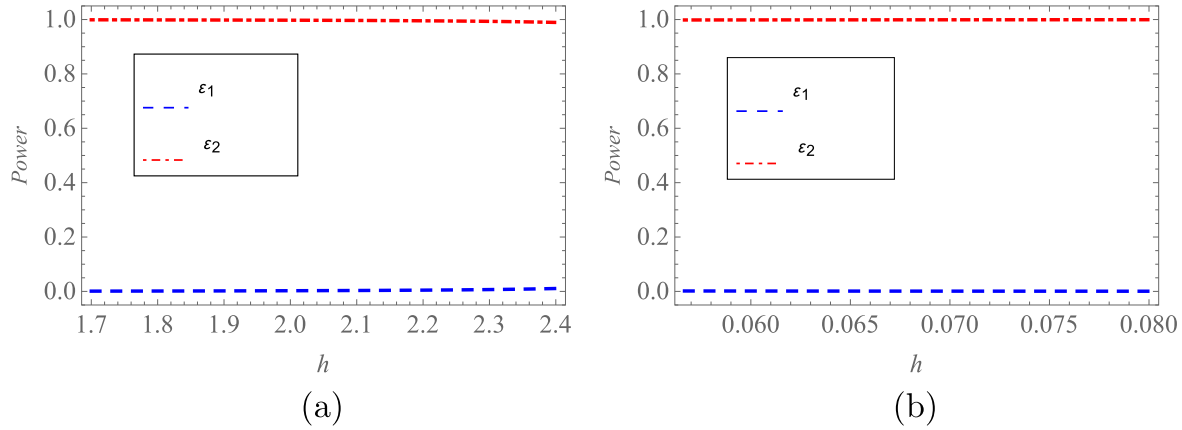

Figure 9. Power flux plotted against h in (a) the transparency and (b) the non-transparency regions.

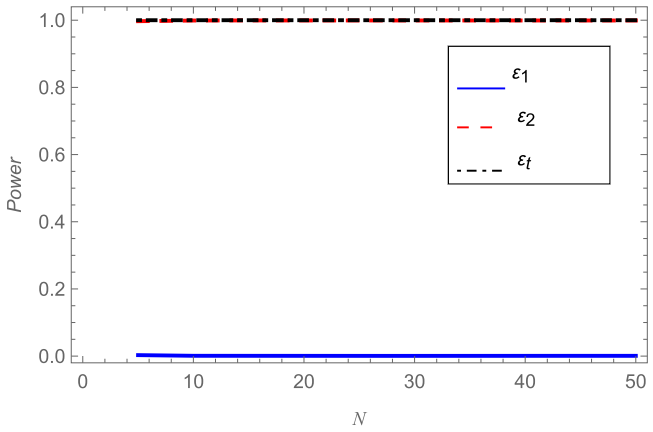

Figure 10. Power flux plotted against truncated terms N.

respectively. Figures 7(a), 8(a) and 9(a) display the behavior of energy flux against the respective duct heights a, b and h in the transparency regime. Figures 7(b), 8(b) and 9(b) present this behavior in the non-transparency regime. These figures conclude that the power balance identity (equation (65)), mentioned in section 4, is achieved by the mode-matching solution for varying duct heights. The differences in the transparency and non-transparency regions are noticed as differences in heights only. It is observed from the figures that total transmission takes place with respect to the increase in heights. The only fluctuation in transmission is observed in heights a and b in the non-transparency regime.

Table 1. Cut-on modes.

Height (a)	Region 1	Region 2	Region 3	Region 4
0.02	2	5	1	2
1.6	2	5	2	2

For the graphs plotted against heights, the values of $\overline{a}$, $\overline{b}$ and $\overline{h}$ are considered between $0.001 < \overline{a} < 0.084$ cm, $1 < \overline{b} < 4$ and $0.085 < \overline{h} < 0.12$, respectively. Figure 10 depicts the variation of the modulus of powers versus the truncation number N. It is evident from the figure, as well as table 3, that the effect of the truncation is insignificant for $N \geqslant 45$. Therefore, the infinite system of algebraic equations for this case can be easily dealt with as finite.

5.2. Case II

To establish the validity of the proposed solution and to provide physical insight into the given problem, the system

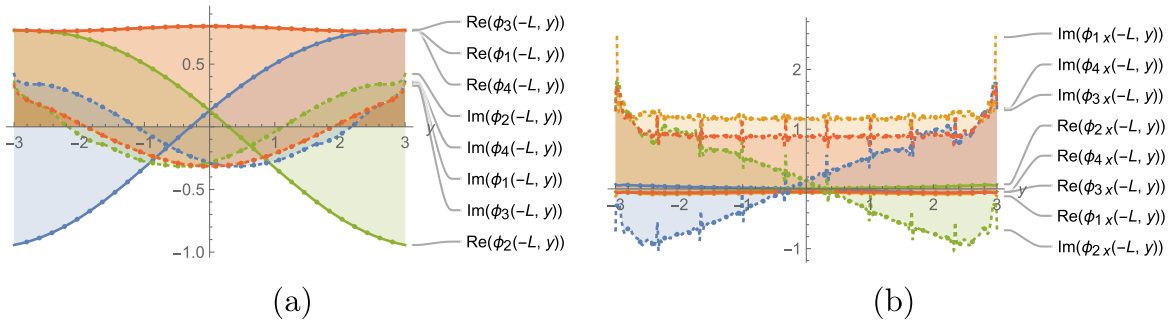

Figure 11. The real and imaginary parts of the (a) magnetic and (b) electric fields at $x = -L$, $-h < y < h$.

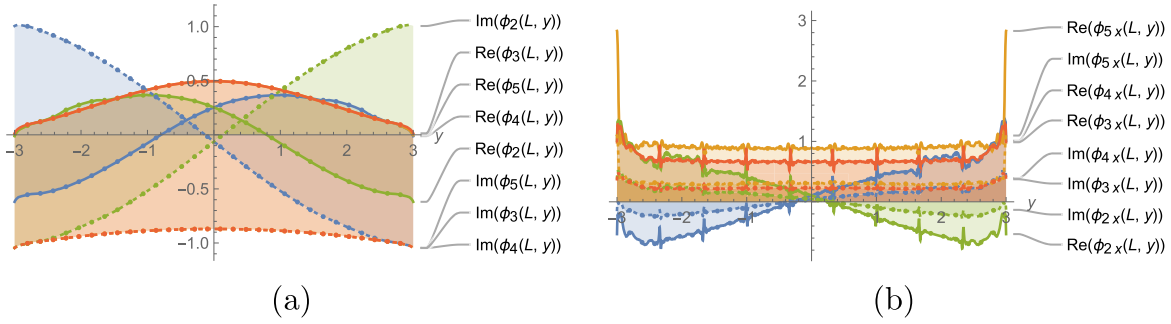

Figure 12. The real and imaginary parts of the (a) magnetic and (b) electric fields at $x = L$, $-h < y < h$.

Table 2. Cut-on modes.

Height (b)	Region 1	Region 2	Region 3	Region 4
20	2	7	1	2
24	2	8	1	2

Table 3. Convergence through truncation.

Terms (N)	$\mathcal{E}_1$	$\mathcal{E}_2$	$\mathcal{E}_t$
5	0.002 922	0.997 078	1
10	0.000 951	0.999 049	1
15	0.000 624	0.999 376	1
20	0.000 760	0.999 240	1
25	0.000 746	0.999 254	1
30	0.000 783	0.999 217	1
35	0.000 816	0.999 184	1
40	0.000 817	0.999 183	1
45	0.000 847	0.999 153	1
50	0.000 847	0.999 153	1

revealed in equations (47), (48), (54) and (55) is truncated up to 70 terms. Figures 11(a) and (b) reflect the cogency of real and imaginary parts of the magnetic field ϕ_i and the electric field $\phi_{ix} = \dfrac{\partial \phi_i}{\partial x}$, $i = 1, 2, 3, 4$ at the interface $x = -L$. The perfect agreement of the components of these fields ϕ_j and $\phi_{jx} = \dfrac{\partial \phi_j}{\partial x}$, $j = 2, 3, 4, 5$ at the interface $x = L$ is exhibited in figures 12(a) and (b). It is obvious that the truncated solution reconstructs the matching conditions of the magnetic and electric fields.

The duct heights are specified as $\overline{b} = 0.5$ cm, $\overline{a} = 0.4$ cm, $\overline{h} = 0.45$ cm. The length of the groove is set to $2\overline{L} = 2 \times 0.42$ cm. The plasma frequency is fixed as $\omega_p = 10^9$.

6. Concluding remarks

A detailed investigation of the propagation of electromagnetic waves in a parallel-plate rectangular waveguide with a groove, with a slab of cold plasma in its center, has been conducted. The study was focused to investigate a structure with a view to its use as a plasma waveguide resonator and gas chromatography equipment. These designs can also be applied in plasma antennas, halfway plates and frequency selective surfaces. The reflection and transmission analysis in this paper may find use in reflective-type halfway plates and transmission control in quarter-wave plate and half-wave plate metallic and all-dielectric metasurfaces [44, 45]. The physical configuration includes a groove enclosed between two semi-bounded waveguides. The left and right sections of the waveguide were composed of semi-bounded regions $x < -L$ and $x > L$, respectively, with a metallic wall of height $2h$ and with a dielectric. The central section is a bounded metallic groove $|x| < L$, with height $2b$. It contains a slab of cold plasma, with height $2a$, (I) bounded by metallic strips, and (II) embedded between dielectric layers without metallic strips. The boundary value problems corresponding to reflection and transmission for both cases were formed into systems of infinite algebraic equations.

The results obtained for case (I) were compared with numerical deductions presented by Najari *et al*. The mode-matching solution was explored to analyze the behavior of transmission and reflection coefficients for the first three incident modes in the transparency and non-transparency regimes. The first mode of the reflected wave remains dominant in the transparency and non-transparency regimes. It is also concluded that the first transmitted mode is dominant in both frequency regimes. The magnitudes of the reflection and transmission coefficients for modes other than the dominant mode are negligible in the non-transparency region.

The energy flux in different duct sections is also analyzed for both transparency and non-transparency cases. The energy propagates for both cases with the changes in the heights of the waveguide, while reflection remains negligible with the increase in the heights. The conservation of power establishes the convergence and accuracy of the proposed solution.

This work can be extended in the form of a symmetric rectangular waveguide with more than one plasma slab embedded between metallic conducting plates or dielectric layers inside the groove. A structure with periodic grooves with plasma slabs sandwiched between layers of dielectric material can also be discussed.

Competing interests

The authors declare that they have no competing interests.

References

[1] Chen Z, Chen G, Obenchain R, Zhang R, Bai F, Fang T, Wang H, Lu Y, Wirz R E and Gu Z 2022 Cold atmospheric plasma delivery for biomedical applications *Mater. Today* **54** 153–88

[2] Privat-Maldonado A, Bengtson C, Razzokov J, Smits E and Bogaerts A 2019 Modifying the tumour microenvironment: challenges and future perspectives for anticancer plasma treatments *Cancers* **11** 1920

[3] Jasinski M, Dors M and Mizeraczyk J 2008 Production of hydrogen via methane reforming using atmospheric pressure microwave plasma *J. Power Sources* **181** 41–5

[4] Wait J R 1961 Some boundary value problems involving plasma *J. Res. Natl Bur. Stand.: Math. Math. Phys.* **65B** 137–50

[5] Tiryakioglu B 2020 Mode matching analysis of sound waves in an infinite pipe with perforated screen *Acoust. Phys.* **66** 580–6

[6] Alahmadi H N, Nawaz R, Alkinidri M and Alruwaili A D 2022 Noise control from dual air cavity membranes in a rigid waveguide *Meccanica* **57** 3023–32

[7] Tiryakioglu B 2021 Sound radiation from non-uniformly lined duct with partial rigidity *Comput. Math. Math. Phys.* **61** 2118–28

[8] Shafique S, Afzal M and Nawaz R 2017 On mode-matching analysis of fluid-structure coupled wave scattering between two flexible waveguides *Can. J. Phys.* **95** 581–9

[9] Alahmadi H, Afsar H, Nawaz R and Alkinidri M O 2022 Scattering characteristics through multiple regions of the wave-bearing trifurcated waveguide *Waves Random Complex Medium* 1–17

[10] Alkinidri M, Hussain S and Nawaz R 2023 Analysis of noise attenuation through soft vibrating barriers: an analytical investigation *AIMS Mathematics* **8** 18066–87

[11] Shen H M 1991 Plasma waveguide: a concept to transfer electromagnetic energy in space *J. Appl. Phys.* **69** 6827–35

[12] Shivarova A and Zhelyazkov I 1978 Surface waves in a homogeneous plasma sharply bounded by a dielectric *Plasma Phys.* **20** 1049

[13] Alekhina T Y and Tyukhtin A V 2011 Electromagnetic field of a charge intersecting a cold plasma boundary in a waveguide *Phys. Rev.* E **83** 066401

[14] Liu M 2020 Four-layer tunable wideband electromagnetic shield based on cold plasma *IEEE Access* **8** 171621 171621–7

[15] Young J L and Full A 1994 Finite difference time domain implementation for radio wave propagation in a plasma *Radio Sci.* **29** 1513–22

[16] Gehre O, Mayer H and Tutter M 1972 Propagation of microwaves in a circular waveguide partially filled with a cold plasma dielectric *Zeitschrift fur Naturforschung* A **27** 215–21

[17] Khalil S M and Mousa N M 2014 Dispersion characteristics of plasma-filled cylindrical waveguide *J. Theor. Appl. Phys.* **8** 1–14

[18] Dvorak S L, Ziolkowski R W and Dudley D G 1997 Ultra-wideband electromagnetic pulse propagation in a homogeneous, cold plasma *Radio Sci.* **32** 239–50

[19] Jazi B, Rahmani Z and Shokri B 2013 Reflection and absorption of electromagnetic wave propagation in an inhomogeneous dissipative magnetized plasma slab *IEEE Trans. Plasma Sci.* **41** 290–5

[20] Geng Y, Wu X and Li L 2003 Analysis of electromagnetic scattering by a plasma anisotropic sphere *Radio Sci.* **38** 12-1–12-12

[21] Sui J, Dong R, Liao S, Zhao Z, Wang Y and Zhang H F 2023 Janus metastructure based on magnetized plasma material with and logic gate and multiple physical quantity detection *Ann. Phys.* **535** 2200509

[22] Sui J, Liao S, Dong R and Zhang H F 2023 A janus logic gate with sensing function *Ann. Phys.* **535** 2200661

[23] Ikegami H 1968 Scattering of microwaves from a plasma column in rectangular waveguide *Jpn. J. Appl. Phys.* **7** 634

[24] Cicconi G, Molinari V G and Rosatelli C 1973 Microwave reflection from a plasma column in a rectangular waveguide *Jpn. J. Appl. Phys.* **12** 721

[25] Yee K 1966 Numerical solution of initial boundary value problems involving Maxwell's equations in isotropic media *IEEE Trans. Antennas Propag.* **14** 302–7

[26] Li P and Jiang L J 2013 Simulation of electromagnetic waves in the magnetized cold plasma by a DGFETD method *IEEE Antennas Wirel. Propag. Lett.* **12** 1244–7

[27] Xiu D and Karniadakis G E 2002 The Wiener–Askey polynomial chaos for stochastic differential equations *SIAM J. Sci. Comput.* **24** 619–44

[28] Yang Q, Wei B, Li L and Ge D 2018 Simulation of electromagnetic waves in a magnetized cold plasma by the SO-DGTD method *IEEE Trans. Antennas Propag.* **66** 4151–7

[29] Mur G 1981 Absorbing boundary conditions for the finite-difference approximation of the time-domain electromagnetic-field equations *IEEE Trans. Electromagn. Compat.* **4** 377–82

[30] Tan T, Taflove A and Backman V 2012 Single realization stochastic FDTD for weak scattering waves in biological random media *IEEE Trans. Antennas Propag.* **61** 818–28

[31] Smith S M and Furse C 2012 Stochastic FDTD for analysis of statistical variation in electromagnetic fields *IEEE Trans. Antennas Propag.* **60** 3343–50

[32] Samimi A and Simpson J J 2014 An efficient 3-D FDTD model of electromagnetic wave propagation in magnetized plasma *IEEE Trans. Antennas Propag.* **63** 269–79
[33] Fang Y, Liu J-F, Jiao Z-H, Bai G-H and Xi X-L 2018 A 3-D stochastic FDTD algorithm for wave propagation in isotropic cold plasma medium based on bilinear transform *IEEE Trans. Plasma Sci.* **47** 173–8
[34] Liu J F, Wang J, Fang Y, Pu Y R and Xi X L 2018 An unconditionally stable stochastic WLP-FDTD algorithm for wave propagation in isotropic cold plasma media *IEEE Microwave Wireless Compon. Lett.* **28** 852–4
[35] Fang Y, Xi X L, Wu J M, Liu J F and Pu Y R 2016 A JE collocated WLP-FDTD model of wave propagation in isotropic cold plasma *IEEE Trans. Microwave Theory Tech.* **64** 1957–65
[36] Mittra R and Lee S W 1967 Mode matching method for anisotropic guides *Radio Sci.* **2** 937–42
[37] Liu Y H and Li H F 2009 An application of the mode-matching technique in the calculation of resonators in gyro-devices *Nucl. Instrum. Methods Phys. Res., Sect. A* **598** 605–10
[38] Najari S, Jazi B and Jahanbakht S 2021 The mode generation due to the wave transmission phenomena from a loss free isotropic cylindrical metallic waveguide to the semi-bounded plasma waveguide *Waves Random Complex Medium* **31** 1287–302
[39] Rao S, Fu H, Zhang J, Zhang D and Zhang H 2022 Tunable phase retarder of 1D layered photonic structure combining nonlinear Kerr dielectric defect layers and magnetized plasma materials *Ann. Phys.* **534** 2200337
[40] Ishimaru A 2017 *Electromagnetic Wave Propagation, Radiation, and Scattering: From Fundamentals to Applications* (Wiley)
[41] Ayub M, Khan T A and Jilani K 2016 Effect of cold plasma permittivity on the radiation of the dominant TEM-wave by an impedance loaded parallel-plate waveguide radiator *Math. Methods Appl. Sci.* **39** 134–43
[42] Cojocaru E 2010 Modes in dielectric or ferrite gyrotropic slab and circular waveguides, longitudinally magnetized, with open and completely or partially filled wall *JOSA*B **27** 1965–77
[43] Swanson D G 2003 *Plasma Waves* (CRC Press) II edn
[44] Zhou G, Zhu B, Zhao J, Zhu G, Jin B, Feng Y, Kang L, Xu W, Chen J and Wu P 2017 A broadband reflective-type half-wave plate employing optical feedbacks *Sci. Rep.* **7** 9103
[45] Yahyaoui A, Rmili H, Achouri K, Sheikh M, Dobaie A, Affandi A and Aguili T 2017 Transmission control of electromagnetic waves by using quarter-wave plate and half-wave plate all-dielectric metasurfaces based on elliptic dielectric resonators *Int. J. Antennas Propagation* **2017** 8215291